

Dynamic Response of LDX 2404® Duplex Stainless Steel to Uniaxial Shock Loading

Raymond F Miller¹

University of New South Wales at the Australian Defence Force Academy

Symmetric plate-impact experiments have been performed on LDX2404® Duplex Stainless Steel to investigate its response to shock-loading. Three Shock Recovery Experiments have been performed at peak stresses of 20GPa, 15GPa, and 10GPa in a single-stage light gas gun. For each experiment an LDX2404® sample was housed in a Shock-Recovery Assembly of concentric rings and axial interfaces to ensure any microstructural changes were due to shock loading alone. Microstructural characterisation of post-mortem samples was performed using Optical Microscopy, X-Ray Diffraction, Electron Back-Scatter Diffraction, and micro-hardness testing. Significant increases in hardness have been observed in the 20GPa and 15GPa samples indicating the occurrence of the $\alpha \rightarrow \epsilon\text{-Fe} \rightarrow \alpha$ phase transformation-reverse transformation. Small volume fractions of $\gamma \rightarrow \epsilon$ -martensite phase transformations have been identified in the austenite regions in both the 20GPa and 15GPa samples.

Contents

I. Introduction	2
II. Experimental Method	
A. Design, Manufacture and Assembly of Shock-Recovery Assembly Components	2
B. Plate Impact Experiments	3
C. Sample Recovery and Preparation	3
D. Characterisation	3
III. Results	
A. Visual analysis and measurements	4
B. PDV	4
C. Optical Microscopy	5
D. Hardness Testing	6
E. X-Ray Diffraction	6
F. EBSD	7
IV. Discussion	
A. Dynamic response	7
B. Shock-recovery assembly	9
V. Conclusion	9
VI. Recommendations	10
References	11

APPENDICES

Appendix A. Outokumpu material test certificate for the as-received LDX2404®	A1
Appendix B. Calculations for Shock-Recovery Assembly Design	B1
Appendix C. CAD Drawing of Shock-Recovery Assembly	C1
Appendix D. Shock-Recovery Assembly – Assembly Process	D1
Appendix E. Post-mortem Sample Preparation Process	E1
Appendix F. Hardness testing results	F1
Appendix G. XRD refinement plots and data	G1
Appendix H. FSV calculations from PDV data and comparison to Velocimeter	H1

¹ CAPT, School of Engineering & Information Technology. ZEIT4500.

Nomenclature

EBSD	= Electron Back-Scatter Diffraction
XRD	= X-Ray Diffraction
OM	= Optical Microscopy
HEL	= Hugoniot Elastic Limit

I. Introduction

Duplex Stainless Steels (DSS) are a group of stainless steels that consist of two phases, namely ferrite and austenite, that provide greater strength and corrosion resistance than single phase stainless steels. LDX 2404® is one of the newest DSSs, and with its approximately equal volume fractions of austenite and ferrite, displays the enhanced mechanical properties listed in Table 1.

Table 1. Average mechanical properties of LDX 2404® compared to other DSSs and common single-phase stainless steels [3].

Material	Yield strength (MPa)	Tensile strength (MPa)	Elongation (%)	Hardness (HRB)
LDX 2404®	640	850	30	102
LDX 2101®	610	810	46	99
2205 DX	690	880	47	101
304	285	640	70	82

interest. While there are numerous reports on the shock response of single-phase stainless steels, the response of DSS to shock loading is yet to be determined.

II. Experimental Methods

The as-received LDX 2404® has been hot-rolled and heat treated to a minimum of 1040 °C by Outokumpu before being quenched with forced air and water[3]. The material is supplied in A4 size sheets that are 6 mm nominal thickness. A copy of the as-received materials testing certificate produced by Outokumpu is attached at Appendix A.

A. Design, Manufacture and Assembly of Shock-Recovery Assembly Components

The design of the Shock-Recovery Assembly (SRA) was based on similar assemblies reported on by Bourne and Gray, with modifications to suit experimental constraints including a maximum target assembly diameter of 70mm [4]. Equations derived by Orava and Wittman were used to calculate the minimum width of momentum trap rings and thickness of spall plates [5]. Calculations for the SRA are attached at Appendix B.

SRA components were machined from both LDX 2404® and LDX 2101 hot-rolled plates. The acoustic impedance of the two DSSs ($3.35 \times 10^7 \text{ kg/m}^2\text{s}$ for LDX2404 and $3.46 \times 10^7 \text{ kg/m}^2\text{s}$ for LDX2101) is very similar making LDX 2101 suitable for some of the components considering the limited quantity of LDX 2404® available [6]. The components were wire-cut out of the as-received plates using an Electronic Discharge Machine (EDM) and then surface ground to the finished dimensions. These machining processes were used as they impart minimal machining stresses when sufficient coolant is used. An assembly drawing detailing all components in the SRA is attached at Appendix C.

The assembly process was completed using a Shimadzu AG-X 50 kN press. A very light coating of Molybdenum disulphide grease was applied to the mating surfaces during assembly. The assembly process, detailed in Appendix D, was developed and refined during assembly. Both sides of the SRA were surface ground after assembly.

Shock loading is the process where a body is subjected to rapid impulsive loading whose time of application is short compared with the time for the body to respond inertially [1]. Shock-Recovery Experiments are a specific technique developed to assess the residual effects of shock-wave compression on a materials microstructure [2]. A Shock-Recovery Assembly is an assembly of concentric rings and interfaces that prevent unwanted effects of shock loading, including radial release waves and spallation, from entering or occurring in the sample of

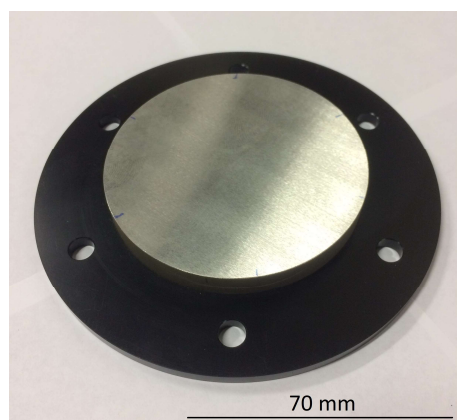


Image 1. SRA in Delrin mounting plate.

B. Plate Impact Experiments

A Polyurethane resin foam sabot was prepared for each flyer with a step machined into the face to provide a free-surface for the flyer. A vent hole was drilled in the sabot to allow equilibrium pressure conditions on both sides of the flyer when the bore of the gun is evacuated to 0.8 mBar. The LDX 2404® flyers were lapped after surface grinding to reduce taper across the thickness to < 0.5 mRad. The flyers were then set into the sabot using a low-viscosity epoxy and the alignment of the flyer face to the sabot axis was checked using a Mitutoyo dial indicator. A flyer face angle of < 0.5 mRad measured perpendicular to the axis of the sabot was achieved for all projectiles.

A Delrin mounting plate was used to mount the SRA on the gun. The assembled and surface-ground SRA was set into the Delrin mounting plate using low-viscosity epoxy as seen in Image 1. A Delrin backing plate with clearance hole for the sample to pass through was used to mount the PDV probe. The mounting hole was machined to position the PDV probe with a 1.5 mm gap between the probe and the rear surface of the PDV Sample.

The SRA and Delrin mounting plate were mounted onto the end of the barrel using three mounting studs and aligned with the axis of the barrel using a laser. The smaller secondary chamber was mounted onto the flange on the end of the barrel and the PDV probe cable was passed through a port in the chamber. A sheet of Mylar was fitted between the end of the chamber and an O-ring sealed retaining plate.

The sabot was mounted onto the plunger in the receiver of the gas gun. A catch can in the primary chamber was stuffed with rags to facilitate soft-recovery of the components. Thiot software was used to calculate the reservoir pressure for the required velocity for each shot. The primary chamber was evacuated to 200 mbar and the secondary chamber to 0.8 mbar. A Symes VMS 2000B velocimeter with a twin collimator mounted in the secondary chamber was used to record the velocity of the projectile immediately before impact. A Tektronix DPO 7354C Digital Phosphor Oscilloscope was used to record the PDV signal.

C. Sample Recovery and Preparation

The components were soft-recovered in rags in a catch can mounted in the primary chamber. The components were inspected and measured for residual strain, spall plane location, and plastic deformation. The Sample plate, Spall plates, and Cover plate were all cut in half, parallel to the transverse (TD) plane, using a low speed diamond saw. Sample halves were set in Struers EpoFix Resin and then ground and polished using the process detailed in Appendix E.

D. Characterisation

The microstructure of the as-received LDX 2404® has been studied by Ameri et al [6]. The FCC phase has high-angle grain boundaries (HAGB) ranging from 25° to 60°, with the dominant misorientation angle being 60°[6]. As a result of the HAGB, annealing $\Sigma 3$ twins exist along grain boundaries[6]. The BCC phase has a wider distribution of grain angle boundaries ranging from 5° to 60°, with the dominant misorientation angle being less than 15°[6]. Average ferrite grain size is 26 μm while the average austenite grain size is 18 μm when the annealing twins are excluded, or 20 μm when included[6].

X-Ray diffraction (XRD) scans were conducted on the as-received sample as well as post-mortem samples using a Malvern Panalytical Empyrean diffractometer. For all scans, a $\frac{1}{4}$ inch primary slit was used with a 2 theta range of 35° to 110°, 0.0131 degree step size, 150.45 s/step, 45 kV and 40 mA settings. While the primary slit size would have resulted in the epoxy being scanned in the smaller 2 theta range, the amorphous structure of the epoxy mould resulted in no Bragg peaks being associated with the epoxy. Refinement of the XRD data was completed using Fullprof software version 5.60 with a [110] preferred orientation for the as-received sample due primarily to its hot-rolled manufacturing method.

The as-received and post-mortem samples were etched to identify phases using Beraha etchant for 30 – 60 seconds. Two other etchants were trialled including mixed acids (HCl, HNO₃, and Acetic acid) for grain boundaries and Glyceregia (HCl, Glycerol, and HNO₃). While the Beraha etchant does damage the ferrite phase, it was the only etchant out of the three that was effective at generating a distinctive surface. OM images of the etched samples were taken with a Zeiss AXIO microscope.

Hardness testing of the as-received and post-mortem samples was completed using a Shimadzu Micro Hardness Tester with a force of 98.07 mN and 10 second holding time. The shocked samples were hardness tested at 0.5mm, 1.5mm and 2.5mm along the shock axis in the centre of the sample (central axis) as well as at a 6mm radial distance from the central axis.

EBSD scans were taken of the 20GPa and 15GPa samples near the central axis of the sample and at a radial distance from the central axis and with a range of step sizes from 1 μm down to 0.01 μm . Orientation Imaging Microscopy (OIM) software was used for analysis of the EBSD data.

III. Results

A. Visual Analysis and Measurements

All target holders and secondary momentum trap rings (MTR2) have spall planes that coincide with the theoretical spall plane location on the X-t diagrams for respective impact velocities, as indicated in Figure 1. The thickness of the post-mortem sample plates was measured and compared to the original thickness. The residual strain of each sample plate has been calculated as $0.99\% \pm 0.1\%$, $0.30\% \pm 0.15\%$, and $0.03\% \pm 0.28\%$ for the 20GPa, 15GPa, and 10GPa shocked samples respectively. The details for the residual strain measurements and calculations are listed in Table 2.

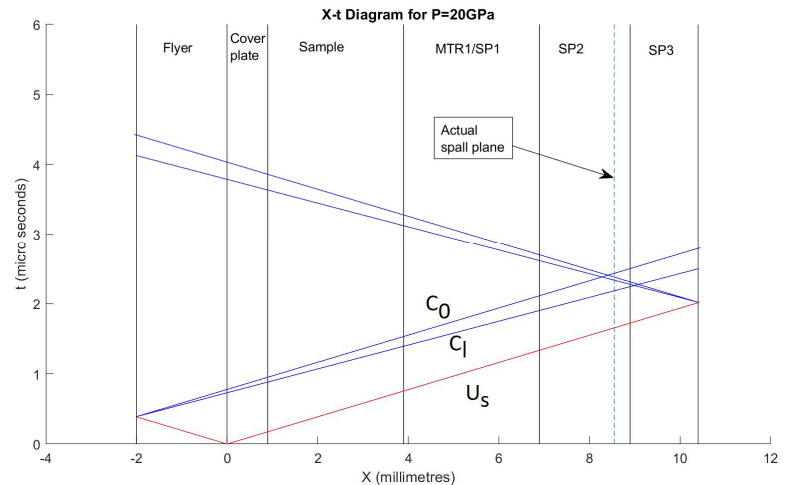


Figure 1. X-t diagram for 20GPa shock experiment.

U peak (m/s)	σ peak (GPa)	Post-mortem thickness T (mm)							T 0 (mm)	$\Delta T 0$ (mm)	Residual Strain (%)				
		1	2	3	4	5	Ave	ΔT			0.1	0.30	0.99	0.10	
1008	20.1	3.014	3.005	3.004	3.014	3.013	3.010	\pm	0.0020	3.04	\pm	0.01	0.99	\pm	0.10
795	15.3	3.013	3.011	3.010	3.011	3.010	3.011	\pm	0.0006	3.02	\pm	0.01	0.30	\pm	0.15
555	10.2	3.018	3.024	3.016	3.018	3.021	3.019	\pm	0.0016	3.02	\pm	0.01	0.03	\pm	0.28

Table 2. Residual strain for post-mortem sample plates.

B. PDV

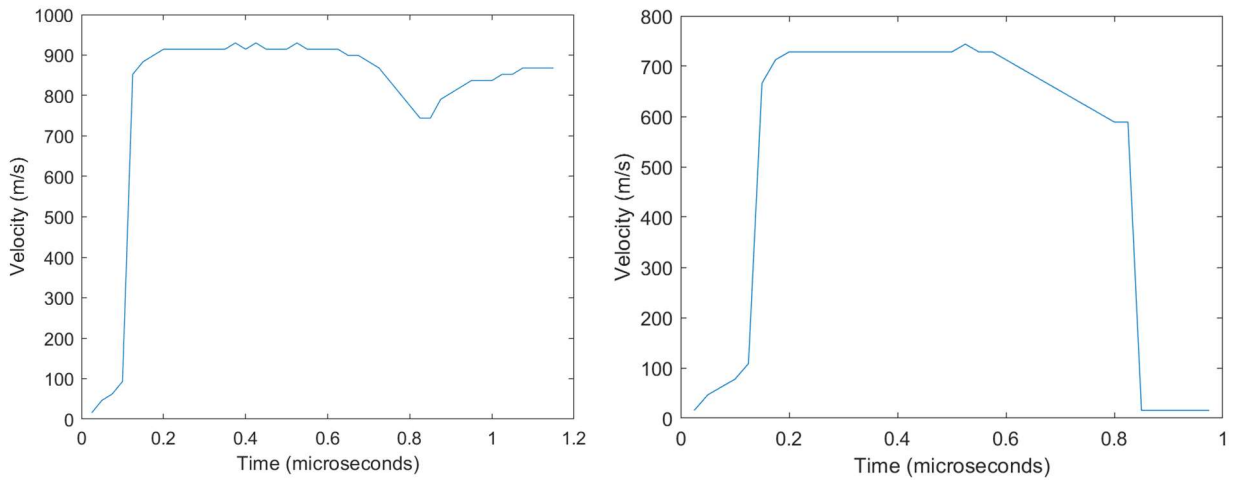


Figure 2. FSV plots for 20GPa peak stress on left and 15GPa peak stress on right.

Free Surface Velocity (FSV) plots have been calculated from the PDV data for each experiment and are shown in Figures 2 and 3. For all experiments the PDV data indicated a lower velocity than that recorded by the velocimeter and a higher velocity than that predicted by the Thiot software. The higher velocities recorded by the velocimeter in comparison to the predicted velocities from the Thiot software are believed to be due to a slightly reduced sabot diameter of 69.85mm reducing frictional forces on the projectile.

The HEL, peak stress and pulse duration were calculated from the FSV plots using equations (1) and (2). The values used from the FSV plots and results for each calculation are detailed in Table 3.

The PDV signal for the 10GPa experiment was weak in the rise to the peak. It is believed that the reason for the signal being weak for this part of the FSV was due to the gap between the probe and the rear surface of the PDV sample (1.8mm) being too large for a velocity of 510 m/s. Due to this error, the rise in the 10GPa FSV plot has been edited and can be seen in Figure 3. The HEL has not been calculated for the 10GPa test due to the uncertainty in the rise portion of the FSV plot. FSV calculations and comparison between FSV from PDV data versus Velocimeter are contained in Appendix H.

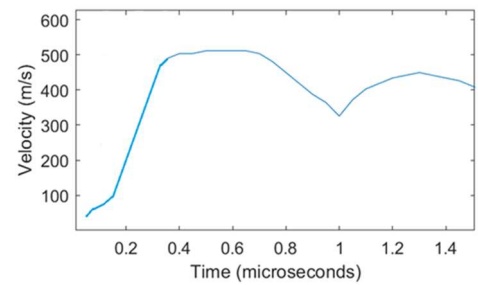


Figure 3. FSV plot for 10GPa peak stress.

Exp #	U HEL (m/s)	U peak (m/s)	C 0 (km/s)	C 1 (km/s)	ρ (kg/m^3)	σ HEL (GPa)	U s (km/s)	σ peak (GPa)
1	90	930	4.351	5.883	7700	2.04	5.1	18.3
2	110	740	4.351	5.883	7700	2.49	4.9	14.1
3	-	510	4.351	5.883	7700	-	4.8	9.4

Table 3. Calculated values for HEL and peak stress from FSV plot.

C. Optical Microscopy

Samples were etched with Beraha etchant for 30 - 60 seconds prior to performing OM. Micro-cracking was observed within the ferrite phase regions in the as-received sample as well as all shocked samples with the shocked samples showing an increase in micro-cracking. The micro-cracking was typically evenly distributed across the samples; however, was predominantly within the smaller ferrite regions between austenite regions and along phase boundaries. Larger ferrite regions typically displayed minor micro-cracking near the edges or no cracking at all.

Heterogenous deformation within the austenite phase was observed at 20GPa and 15GPa with a slightly higher fraction present in the 20GPa sample. This deformation has the appearance of stacking faults or ϵ -martensite plates as can be seen in Images 2 and 3. The deformation in the austenite phase at 20GPa was predominantly observed in regions of the sample that displayed little or no deformation in the ferrite phase.

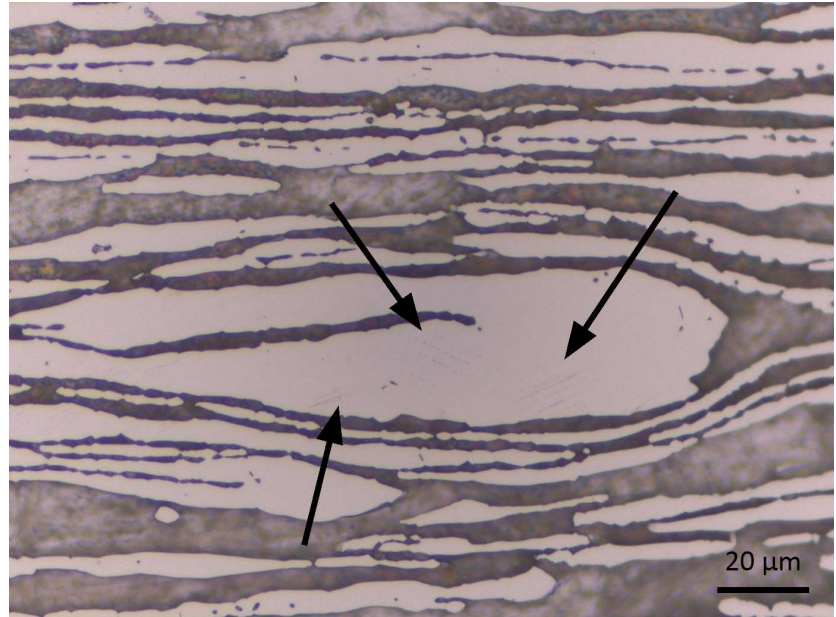


Image 2. Deformation in austenite (light coloured) phase in 20 GPa shocked sample.

$$\sigma_{HEL} = \frac{\rho_0 C_l U_{HEL}}{2} \quad (1)$$

$$\sigma_{peak} = \frac{\rho_0 U_s U_p}{2} \quad (2)$$

$$U_s = \rho_0 U_s U_p \quad (3)$$

Deformation bands were observed in the ferrite phase of both 20GPa and 15GPa samples as can be seen in Images 4 and 5. Deformation-band distribution in the ferrite phase increased with radial distance from the central shock direction axis and was typically angled at 45 degrees from the central axis toward the outer corners of the rear surface.

A narrow band of voids were observed in the ferrite phase of the 15GPa and 10GPa samples. The bands were located approximately 500 μm from the front face of both samples and was distributed evenly in the

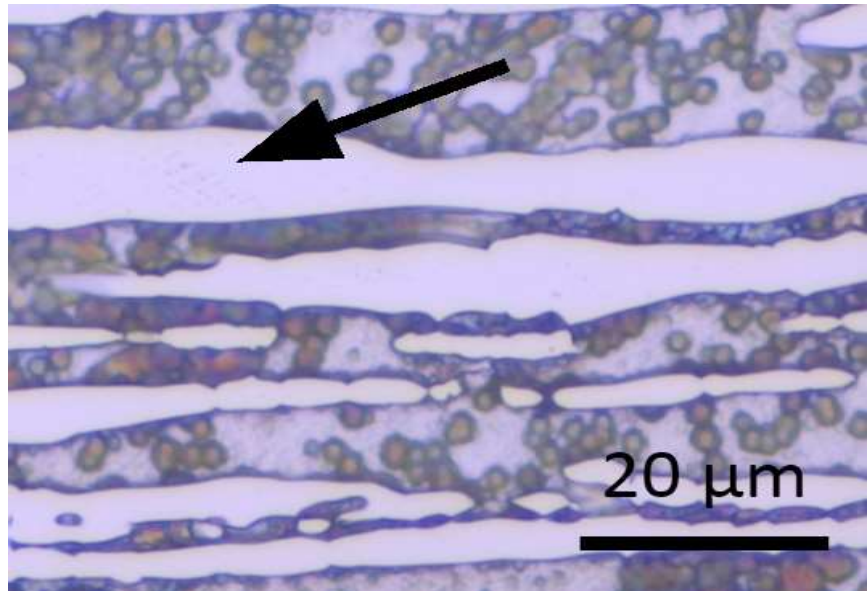


Image 3. Deformation in austenite phase in 15 GPa shocked sample.

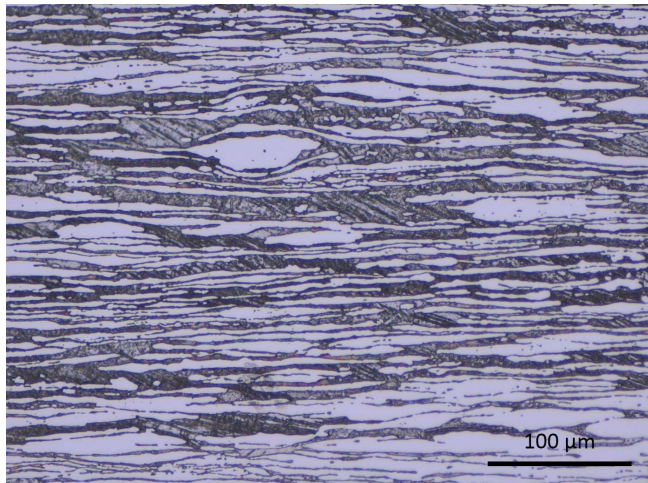


Image 4. Extensive deformation in ferrite (dark) phase of 20 GPa shocked sample.

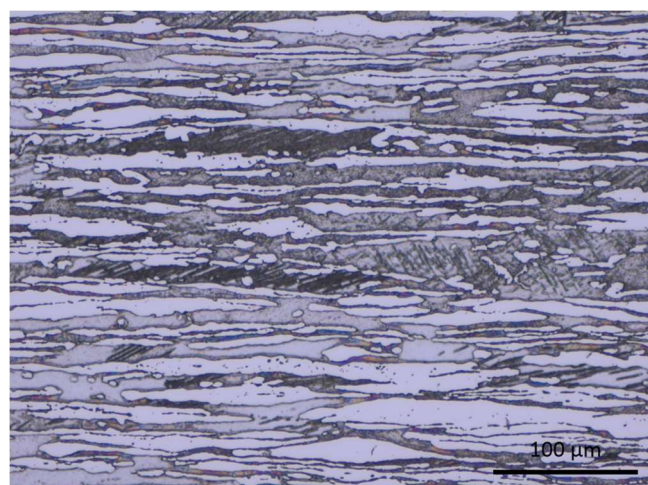


Image 5. Extensive deformation in ferrite (dark) phase of 20 GPa shocked sample.

radial direction, approximately 3.5 mm either side of the central axis of the sample. The band was approximately 200 μm wide in the shock direction. The voids were typically transgranular or along phase boundaries as can be seen in Image 6.



Figure 4. Indicative location of Images 4 and 5 in 20GPa sample. Arrow indicates shock direction. (Not to scale).

D. Hardness Testing

The hardness testing results for both 15GPa and 20GPa samples show increases in hardness within the ferrite regions when compared to the as-received. This increase in hardness from 246 HV \pm 2 HV in the as-received to 274 HV \pm 1 HV and 284 HV \pm 2 HV in the 15GPa and 20GPa samples respectively is consistent in the ferrite regions in both the radial direction and axial direction. The 10GPa sample showed a small increase in hardness to 255 HV \pm 1 HV. Detailed hardness testing results are attached in Appendix F.

E. X-Ray Diffraction

XRD data refinement for the as-received material was completed using a [110] preferred orientation. Volume fractions of 51.84 % ferrite and 48.16 % austenite were observed in the as-

received sample. These results are comparable to the volume fractions of ferrite and austenite reported on by Ameri et al for the as-received LDX 2404® [6].

The refined data analysis using FullProf software for the 20GPa sample suggests a small volume fraction of approximately 1.5% of ϵ -martensite. The refinement for the 20GPa sample had a relatively low chi² of 3.71 and indicated volume fractions of 47.58% α and 50.93% γ . A plot of the XRD data from the 20GPa shocked sample can be seen in Figure 5.

Refinement for the 15GPa sample suggests a slightly higher volume fraction of 4.35% ϵ -martensite; however, the chi² for the 15GPa refinement was higher at 7.91. The volume fractions of ferrite and austenite for the 15GPa refinement were 49.75% and 45.9% respectively. Detailed refinement data and refinement fit plots are attached in Appendix G.

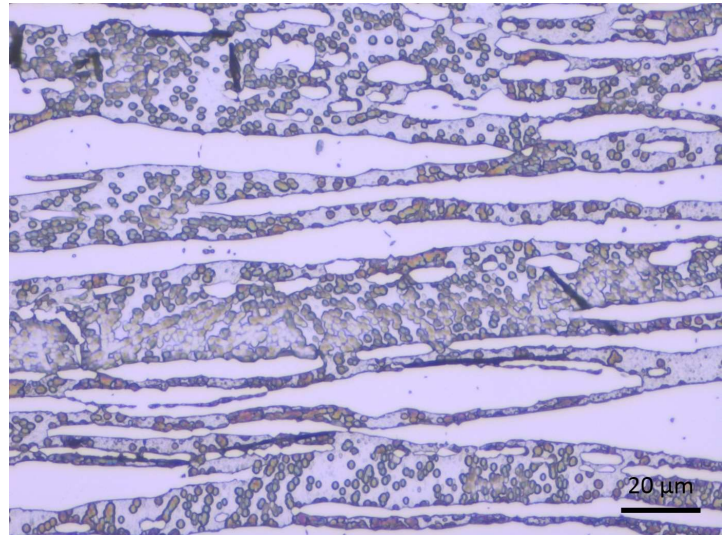


Image 6. Deformation and voids in ferrite phase of 15 GPa shocked sample.

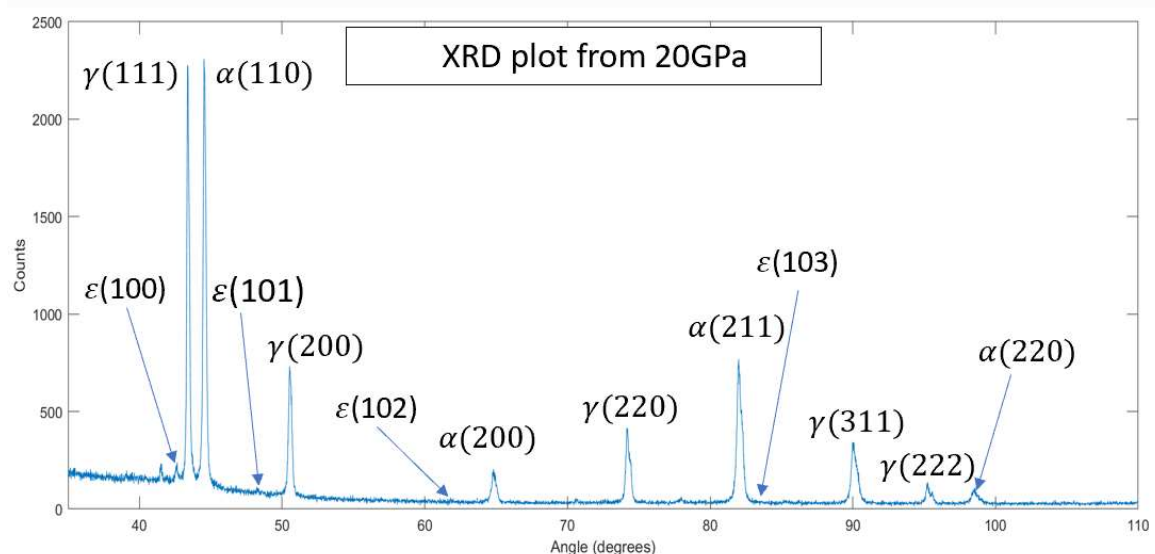


Figure 5. XRD plot from 20GPa shocked sample.

F. EBSD

The EBSD characterisation maps show the possible presence of ϵ -martensite in bands that coincide with the deformation bands in the ferrite phase in both 20GPa and 15GPa samples, as seen in Figure 6. The EBSD maps also show the possible presence of a very small amount of ϵ -martensite in the austenite phase as well; however, most of the ϵ -martensite appears to be located along the previously mentioned deformation bands in the ferrite phase. The inclusion of α' (martensite) phase in the data analysis does yield a significant amount of α' within the ferrite phase in the EBSD map, although α' is not expected to be present in the ferrite phase as it is typically associated with materials that have undergone significant plastic strain [7-9].

IV. Discussion

A. Dynamic Response

Post-mortem analysis of the shocked DSS samples shows the presence of deformation in both ferrite and austenite phases for the 20GPa and 15GPa samples, while deformation appears to be limited to the ferrite phase

of the 10GPa sample. For the 20GPa and 15GPa experiments, the peak stress is typically sufficient to be associated with phase-transformations in single phase BCC (13GPa in iron [10-12]) and single-phase, austenitic stainless steel[9]; however, the ϵ -Fe phase is not stable at ambient pressures and typically undergoes a phase transformation back to α [13]. The deformation in the ferrite phase of the 20GPa sample and 15GPa sample has the appearance of deformation twinning. The $\alpha \rightarrow \epsilon\text{-Fe} \rightarrow \alpha$ process is associated with an increase in deformation twinning[13].

It appears that the ferrite phase in all shocked samples is strengthened significantly by the presence of the austenite in LDX2404®. This is evident by the micro-cracking and deformation bands in the ferrite stopping at the phase boundaries, with the austenite phase appearing to act as a boundary to deformation propagation, as reported on by Ameri et al in spall experiments in LDX 2101[14].

The nature of the deformation in the austenite phase is typical of stacking faults or ϵ -martensite plates; however, OM is not suitable for distinguishing between the two[15]. The formation of ϵ -martensite is reported on as an intermediate step in the indirect phase transformation process $\gamma \rightarrow \epsilon\text{-martensite} \rightarrow \alpha'$ [16-18]; however, the formation of α' is typically associated with strain levels >15%[16] and is not expected to be present in the shocked samples. A relationship between low stacking-fault energy of austenite (γ_{sf}) and the formation of stacking faults and ϵ -martensite plates has been reported on[17]. The exact γ_{sf} of LDX2404® is unknown but is estimated to be <10mJ/m² by comparison of Ni and Cr content to 2205DSS which has a γ_{sf} of 10mJ/m² [16]. This low γ_{sf} for LDX2404® would support the formation of both stacking faults and ϵ -martensite plates.

The limited amount of deformation in the austenite phases in both the 20GPa and 15GPa samples suggests that the austenite is very stable in LDX2404®. The stability of the γ phase in LDX2404® has been estimated using the M_{d30} parameter at -88.2°C using equation (4). This parameter is defined as the temperature at which 50% of the austenite is transformed to α' martensite at 30% strain[18]. By comparison, LDX2101 has a stability of 30.3°C and 304L has a stability of -5.1°C[18], supporting the conclusion that the austenite in LDX2404® is very stable.

$$M_{d30} = 551 - 462(C + N) - 9.2Si - 8.1Mn - 13.7Cr - 29Ni - 29Cu - 18.5Mo \quad (4)$$

A peak stress of 20GPa is sufficient to generate phase transformations in single-phase FCC materials [9], but the amount of ϵ -martensite in the 20GPa sample is very small at approximately 1.5% volume fraction. This could be due to the deformation in the ferrite phase resulting in attenuation of the deviatoric stresses [19] and reducing the associated effect on the austenite. Associated with a small volume fraction of ϵ -martensite plates is the reduced number of intersections and subsequent locations for α' nucleation.

The XRD refinement indicates approximately 1.5% ϵ -martensite in the 20GPa shocked sample and approximately 4.3% ϵ -martensite in the 15GPa shocked sample. These volume fractions correlate well to the small amount of deformation observed in the austenite regions under the optical microscope. However, a volume fraction of >5% ϵ -martensite is generally required to ensure a high degree of confidence in the XRD refinement results[15] and the higher chi² for the 15GPa refinement suggests a lower degree of confidence in the 15GPa refinement in comparison. The indication of the presence of ϵ -martensite in the EBSD map shown in Figure 5 is not conclusive due to the size of the scan region and step size used. Each grain of ϵ -martensite in the map is one pixel in size which is not a sufficient number of pixels to accurately determine the grain type.

The lower FSV calculated from the PDV data for both the 20GPa and 15GPa in comparison to that recorded by the velocimeter could be due to the $\alpha \rightarrow \epsilon$ transformation that occurs at approximately 13GPa. A non-linear relationship between shock wave velocity and particle velocity for polycrystalline iron shocked above the transformation stress of 13GPa has been reported on[11, 20]. This non-linear relationship results in a reduced particle velocity in higher density polycrystalline iron after pressure induced phase transformation[20]. This could explain the reduced FSV calculated from the PDV data; however, the 10GPa FSV is also approximately 6% less than that recorded by the velocimeter without any expected phase transformation occurring at that peak stress magnitude. This suggests that the velocimeter may need re-calibration and that the peak stresses may actually be slightly less.

The FSV plot generated from the PDV data does not indicate the occurrence of any phase transformations. Reports on flyer plate experiments conducted on polycrystalline iron at lower velocities and peak stresses (<400 m/s) indicate a phase transformation in the form of ‘relaxation’ of the FSV plot during the transformation process[20]. It is believed that in the 20GPa and 15GPa experiments the rise from HEL to peak stress was over-driven and the relaxation in the free surface velocity coinciding with the $\alpha \rightarrow \epsilon\text{-Fe}$ transformation at approximately 13GPa did not occur, and therefore does not appear in the FSV plots.

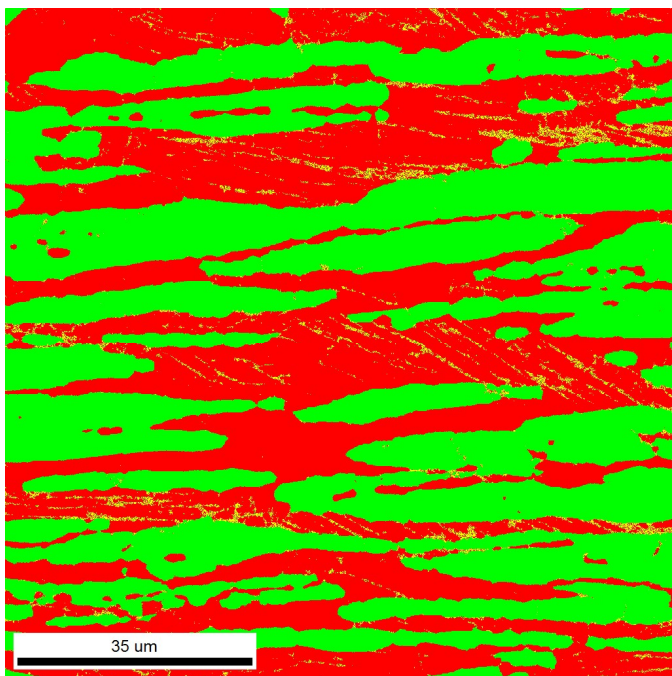


Figure 6. EBSD map of 20GPa sample with α (green), γ (red), and ϵ -martensite (yellow).

have occurred.

Voids in the ferrite phase in the 15GPa and 10 GPa samples appear to be located in the region of potential interaction of release waves in the samples. There were no voids observed under OM in the 20GPa sample, suggesting that the interface between the sample plate and first spall plate in the 15GPa and 10GPa samples may have reflected some of the shock wave as a tensile release wave. This tensile release wave would have interacted with the tensile release wave from the flyer, resulting in incipient spallation in the region that the voids exist.

B. Shock-Recovery Assembly

Residual strain in the 20GPa, 15GPa, and 10GPa samples was calculated as $0.99\% \pm 0.10\%$, $0.30\% \pm 0.15\%$, and $0.03\% \pm 0.28\%$ respectively. For all samples the residual strain is significantly less than the 2% residual strain considered to be a measure of a successful shock-recovery experiment [2, 21, 22]. This very small amount of residual strain suggests that the SRA was successful at trapping radial release waves outside of the sample and the microstructural changes are due to the uniaxial shock loading alone.

The location of the spall plane measured in the Target Holder and MTR/SP1 aligns with the region predicted in the x-t diagram for each velocity as shown for the 20GPa experiment in Figure 1. The presence of what is believed to be incipient spallation in the 15GPa and 10GPa samples suggests that the interface between the sample and first spall plate was not ideal and reflected some of the shock wave as a tensile release wave. It appears that the interface in the 20GPa SRA was suitable as there were no voids observed in the 20GPa.

V. Conclusion

LDX2404® samples have been shock-loaded in a Shock-Recovery Assembly at peak stresses of 20GPa, 15GPa and 10GPa. For all experiments, deformation is predominantly in the ferrite region including deformation bands in the 20GPa and 15GPa shocked samples that stop at the phase boundaries with austenite. The deformation bands in the ferrite have the appearance of mechanical twinning. Optical microscopy images show some damage in the austenite regions of the 20GPa and 15GPa samples with the appearance of stacking faults and ϵ -martensite plates. XRD scans suggest the presence of a small volume fraction, 1.5% and 4.3% of ϵ -martensite, in the 20GPa and 15GPa samples respectively. EBSD scans also suggest a small presence of ϵ -martensite located in the ferrite phase deformation bands.

The small volume fractions of deformation in the austenite phase is attributed to the high stability of the austenite phase in LDX2404® and the attenuation of the deviatoric stresses resulting from the $\alpha \rightarrow \epsilon$ -Fe $\rightarrow \alpha$ phase transformation-reverse transformation that occurs in the ferrite phase at 13GPa. Hardness testing shows a

The effect of undergoing the $\alpha \rightarrow \epsilon$ -Fe $\rightarrow \alpha$ phase transformation and re-transformation has been shown to be evident in the form of increased hardness of the post-mortem microstructure[13]. Hardness testing results indicate an increase in hardness of approximately 15.5% for the 20GPa sample and approximately 11.4 % for the 15GPa sample. This increase in hardness is significant enough to suggest some hardening of the ferrite phase has occurred due to the shock loading. It is believed that this increased hardness is due to the $\alpha \rightarrow \epsilon$ -Fe transformation followed by the ϵ -FE $\rightarrow \alpha$ reverse transformation in iron as the compressed microstructure is released to ambient conditions by the release wave. This process results in additional lattice defects being generated and stored within the ferrite regions and subsequent increase in hardness[13]. The 10GPa shocked sample has a small increase in hardness of approximately 3.7% when compared to the as-received sample. Phase transformations were not expected to occur at 10GPa peak stress and this small increase is not sufficient enough to suggest any phase transformations

significant increase in hardness in the ferrite phase of both the 20GPa and 15GPa samples, supporting the occurrence of the $\alpha \rightarrow \varepsilon$ -Fe \rightarrow α phase transformation-reverse transformation.

The shock-recovery assembly design used in the three experiments appears to have been successful at limiting any effects of radial release waves. The very low residual strains in all experiments (<0.5%) suggest that any deformation within the samples is due to the shock-loading alone. Minor voids occurring in a small region within the 15GPa sample and 10GPa sample may have been due to less than perfect interfaces with the first spall plates.

VI. Recommendations

More analysis of the deformation in the austenite phase is required to confirm the presence of ε -martensite. EBSD scans of smaller regions of interest with a reduced step size need to be conducted on the regions of austenite displaying deformation as well as on the deformation bands in the ferrite phase. More conclusive results can be obtained on potential phase transformations from these scans. Additionally, SEM images may provide further information on the nature of the deformation bands in the ferrite phase.

Further experimentation is required to identify a suitable etchant for LDX2404® that does not damage the ferrite phase. An etchant that works for grain boundaries with LDX2404® is also required to assist in further microstructural analysis.

Future work on LDX2404® could include shock-loading samples at reduced or elevated temperatures to investigate these effects. Also, the effect of orientation to deformation under shock-loading could be tested with samples being shocked in the rolled or transverse direction.

References

1. Gray III, G.T., Follansbee, P.S., Frantz, C.E. , "High-Strain-Rate Deformation: Mechanical Behavior and Deformation Substructures Induced", *Annual Review of Materials Research*, 2012, pp. 285 - 303.
2. Gray III, G.T., Influence of Shock-Wave Deformation on the Structure/Property Behaviour of Materials 1993.
3. Outokumpu, LDX 2404 Duplex Stainless Steel, URL: <http://www.outokumpu.com/en/products-properties/outokumpu-pro-family/forta-range/Pages/default.aspx> [cited 05 Mar 18 2018]
4. Bourne, N.K., Gray, G.T. , Computational design of recovery experiments for ductile materials, *Proceedings of the Royal Society*, Vol. 461. 2005.
5. Orava, R.N., Wittman, R.H., Techniques for the Control and Application of Explosive Shock Waves, *Proceedings: 5th International Conference on High Energy Rate Fabrication*, 1975.
6. Ameri, A.A.H., Brown, A.D., Quadir, Z., Hazell, P., Logos, C., Escobedo-Diaz, J.P. , Investigating the Dynamic Tensile Response of Lean Duplex Stainless Steel and the effects of Radial Release Waves using the Recovered Plate Impact Experiment, *12th International Conference on the Mechanical and Phsyical Behaviour of Materials under Dynamic Loading*, edited by Vol. 183, EPJ Web of Conferences 2017.
7. Okayasu, M., Fukui, H., Ohfuchi, H., Shiraishi, T., Strain-induced martensite formation in austenitic stainless steel, *Journal of Materials Science*, Vol. 48. 2013, pp. 6157 - 6166.
8. Ameri, A.A.H., Escobedo-Diaz, J.P., Quadir, Md. Z., Ashraf, M., Hutchison, W., Strain rate effect on the mechanical response of duplex stainless steel, *Shock Compression Of Condensed Matter*, edited by Vol. 1979(1), 2017.
9. Staudhammer, K.P., Frantz, C.E., Hecker, S.S., Murr, L.E. , Effects of Strain Rate on Deformation-Induced Martensite in 304 Stainless Steel, *International Conference on Metallurgical Effects of Hlgh Strain Rate Deformation and Fabrication*, edited by Murr, M.A.M.a.L.E., Plenum Press, New York, 1981, pp. 91 - 112.
10. Stone, G.A., Orava, R.N., Gray, G.T., Pelton, A.R., An Investigation of the Influence of Shock Wave Profile on the Mechanical Response of Polycrystalline Iron, Rept. SMT-1-78, South Dakota School of Mines and Technology, September 1978 1978
11. Brown, J.M., Fritz, J.N., Hixson, R.S., Hugoniot Data for Iron, *Journal of Applied Physics*, Vol. 88. 2000, pp. 5496-5498.
12. Kadau, K., Germann, T.C., Lomdahl, P.S., Holian, B.L., Cherne, F.J., Atomistic Simulations of Shock-Induced Phase Transitions, *Shock Compression of Condensed Matter*, edited by Vol. 706, American Institute of Physics 2003.
13. Gray III, G.T., High-Strain-Rate Deformation: Mechanical Behavior and Deformation Substructures Induced, *Annual Review of Materials Research*, 2012.
14. Ameri, A.A.H., Escobedo-Diaz, J.P., Quadir, Md.Z., Brown, A., Ashraf, M., Hazell, P. , The Effect of Loading Direction on the Dynamic Damage in Lean Duplex Stainless Steel 2101, *Shock Compression of Condensed Matter*, edited by 2017.
15. Verbeken, K., Van Caenegem, N., Raabe, D. , Identification of Epsilon martensite in a Fe-based shape memory alloy by means of EBSD, *Micron*, Vol. 40. 2009, pp. 151-156.
16. Reick, W., Pohl, M., Padilha, A., Determination of Stacking Fault Energy of Austenite in a Duplex Stainless Steel, *Steel Research*, Vol. 67. 1996, pp. 253 - 256.
17. Eckner, R., Kruger, L., Ullrich, C., Rafaja, D., Schlothauer, T., Heide, G., Microstructure and Mechanical Properties after Shock Wave Loading of Cast CrMnNi TRIP Steel *Metallurgical and Materials Transactions A*, Vol. 47A. 2016, pp. 4922 4932.
18. Xie, L., Huang, T., Wang, Y., Wu, G., Tsuji, N., Huang, X., Deformation Induced Martensitic Transformation and its Initial Microstructure Dependence in a High Alloyed Duplex Stainless Steel *Steel Research International*, Vol. 88. 2017.
19. Meyers, M.A., Murr, L.E., Defect Generation in Shock-Wave Deformation, *Shock Waves and High Strain-Rate Phenomena in Metals - Concepts and Applications*, edited by Meyers, M.A., Murr, L.E., 1981, pp. 753 - 779.
20. Jensen, B.J., Gray III, G.T., Hixson, R.S. , Direct Measurement of the alpha-epsilon Transition Stress and Kinetics for Shocked Iron, *Journal of Applied Physics*, 2009.
21. Gray III, G.T., Follansbee, P.S., Frantz, C.E., Effect of Residual Strain on the Substructure Development and Mechanical Response of Shock-loaded Copper, *Material Science and Engineering*, Vol. A111. 1989.
22. Lassila, D., Gray, G. , Effects of Shock Prestrain on the Dynamic Mechanical Behaviour of Tantalum, *Journal de Physique IV Colloque*, 1991.

Business Unit / QCM

Avesta Works / Johan Nordström

Your ref., Ihre Ref., Votre ref.

test samples

Buyer, Besteller, Acheteur

Outokumpu Nirosta GmbH
Oberschlesienstr. 16
DE 47807, Krefeld
GERMANY

CERTIFICATE - ZEUGNIS - CERTIFICAT

EN 10204-3.1

2453706-EN

Date Datum Date

08-Aug-2017

Load, Ladung, Charge No

SE/150727

Acknowledged ID, Bestätigung, Commande ID

6610/300430287

Invoice No.
Rechnung Nr.

N° de facture

6610/1000556811

Page

Seite

Page

1/1

Requirements, Anforderungen, Exigences

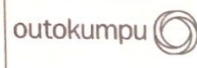
ASTM A 240M-16a

ASME BPVC SEC II PART A SA-240/SA-240M 2015

EN 10088-2:2014

ASTM A 480

Consignee, Empfänger, Lieu de livraison
Outokumpu Stainless AB

Mark of Manufacturer Zeichen des Lieferwerkes Signe de producteur	Process Erschmelzungsart Mode de fusion	Inspector's stamp Zeichen des Sachverständigen Poison de l'expert
	E+AOD	

Grade, Werkstoff, Nuance
Outokumpu Forta LDX 2404
UNS S82441
1.4662

Product, Erzeugnisform, Produit
Stainless Steel Hot Rolled, Coil-Plate
finish 1D, cut edge

Line Reihe Ligne	Item Position Poste	Heat-Lot No Schmelze-Lot Nr Coulée n° - Lot No	Size Abmessungen Dimensions	Pieces Stückzahl Nombre	Quantity / Unit Menge / Einheit Quantité / Unité	
1	4	564159-003	6,00 X 2000 X 1000 mm	1	94 KG	

Chemical composition – Chemische Zusammensetzung – Composition chimiques

Heat	C	Si	Mn	P	S	Cr	Ni	Mo	Cu	N	Ce
	.020	.42	2.93	.025	.001	24.12	3.66	1.61	.34	.273	.00

Radioactive contamination check acc. IAEA recommendations: Approved

Test results – Prüfergebnisse – Results dessais ($1\text{N/mm}^2 = 1 \text{ MPa}$) F = Front – Anfan – Début B = Back – Ende – Fin T = Transverse – Quer – Travers

Test Ref	Temp °C	RP 0.2 N/MM2	RP 1.0 N/MM2	RM N/MM2	A5 %	2" %	HB	FEH
Min	+20	550		750	25	25	HB	%
Max				900			290	
F T	+20	668	739	843	33	33	259	50.0
B T		658	721	831	34	34	260	

Corrosion acc. EN ISO 3651-2A: Approved

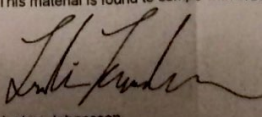
Heat treatment / Solution annealed: Material temp minimum 1040 °C / Quenched (forced air + water)

Steel grade verification (PMI-spectroscopic): Approved

Marking, visual insp. and gauge measurement: Approved

Outokumpu Stainless AB
Business Area Europe
AVESTA WORKS
SWEDEN
Regofice: Stockholm SWEDEN, Regno: 5556001-8748

Telephone: + 46 (0)226 811 73 This material is found to comply with order requirements
Fax: + 46 (0)226 816 46
V.A.T no: SE556001874801


Joakim Johansson
Authorized Inspector



Appendix B - Calculations for Shock-Recovery Assembly Design

1. Required flyer-plate velocity to achieve 20GPa peak stress

Conservation of Momentum: $P - P_0 = \rho_0 U_s U_p$ (1)

Equation of State: LDX2404 $U_s = 4.35 + 1.61 U_p$ (2)

where C_0 for the EoS is given in km/s.

Density: LDX2404 7700 kg/m^3

Just after impact, the pressure at the impact plane in both the target and flyer are equal, i.e. $P_f = P_t$, where the subscript f and t represent flyer and target respectively. Balancing the particle velocities on impact gives $V - U_{P,f} = U_{P,t}$ where V is the flyer velocity at impact and U_p is the particle velocity.

$$\text{Therefore: } V - U_{P,t} = U_{P,f} \quad (3)$$

For a symmetric impact (same flyer and target, or very similar in the case of 2101 and 2404 DSS):

$$U_p = V/2 \quad (4)$$

Substituting equations (2) and (4) into (1) and taking $P_0 = 0$ as the ambient condition yields:

$$P = \rho_0 \left(4.35 + 1.61 \left(\frac{V}{2} \right) \right) \left(\frac{V}{2} \right) \quad (5)$$

For a velocity of 1008 m/s the peak stress is:

$$P = 7700 \text{ kg/m}^3 \left(4.35 \frac{\text{km}}{\text{s}} + 1.61 \left(\frac{1.008 \text{ km/s}}{2} \right) \right) \left(\frac{1.008 \text{ km/s}}{2} \right)$$

$$P = 20.03 \text{ GPa}$$

The shock wave velocity for this impact velocity is:

$$U_s = 4.35 + 1.61 \left(\frac{1.008}{2} \right) = 5.614 \text{ km/s}$$

2. Pulse duration in target with 2mm thick flyer at 1008 m/s impact velocity

Conservation of Mass: $\rho_0 U_s = \rho (U_s - U_p)$ (6)

Pulse duration: $t_p = d_f \left(\frac{1}{U_{s,f}} + \frac{\rho_{0,f}}{\rho_f C_f} \right) + d_c \left(\frac{\rho_{0,c}}{\rho_c C_c} - \frac{1}{U_{s,c}} \right)$ (7)

where the subscripts f and c denote the flyer plate and cover plate respectively.

Rearranging equation (6) for shocked density and substituting into (7) gives:

$$t_p = d_f \left(\frac{1}{U_{s,f}} + \frac{U_{s,f} - U_{p,f}}{U_{s,f} C_f} \right) + d_c \left(\frac{U_{s,c} - U_{p,c}}{U_{s,c} C_c} - \frac{1}{U_{s,c}} \right) \quad (8)$$

Substituting in the values with thickness $d_f = 2\text{mm}$ and $d_c = 2\text{mm}$ into equation (8) gives:

$$t_p = 0.002m \left(\frac{1}{5164\text{m/s}} + \frac{(5164 - 504)\text{m/s}}{(5164 \times 4351)\text{m/s}} \right) + 0.002m \left(\frac{(5164 - 504)\text{m/s}}{(5164 \times 4351)\text{m/s}} - \frac{1}{5162\text{m/s}} \right)$$

Therefore: $t_p = 0.83\mu s$

3. Minimum momentum trap width

Equation: $w \geq \frac{c_t}{c_{0,t}} \left[\left(\frac{U_{s,t} + c_{0,t}}{U_{s,t}} \right) d_f + d_t \right] \quad (9)$

Substituting values into equation (9):

$$w \geq \frac{5883m/s}{4351m/s} \left[\left(\frac{5162m/s + 4351m/s}{5162m/s} \right) 0.002m + 0.003m \right]$$

Therefore: $w \geq 9mm$

4. Minimum spall plate thickness

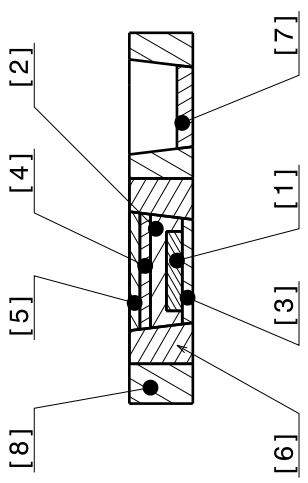
Equation: $h \geq \frac{c_t}{c_{0,t}} \left[\left(\frac{U_{s,f} + c_{0,f}}{U_{s,f} + c_f} \right) d_f + \left(\frac{U_{s,t} - c_{0,t}}{U_{s,t} + c_t} \right) d_t \right] \quad (10)$

Substituting values into equation (10):

$$h \geq \frac{5883m/s}{4351m/s} \left[\left(\frac{5162m/s + 4351m/s}{5162m/s + 5883m/s} \right) 0.002m + \left(\frac{5162m/s - 4351m/s}{5162m/s + 5883m/s} \right) d_t \right]$$

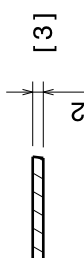
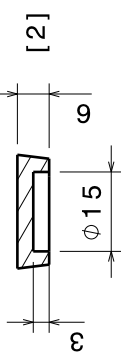
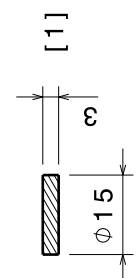
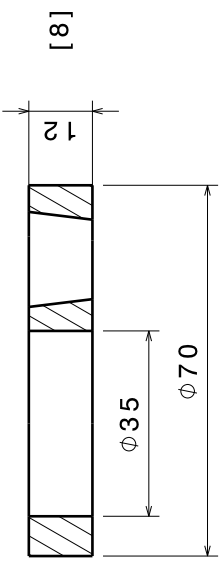
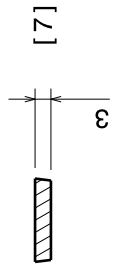
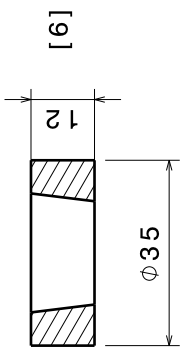
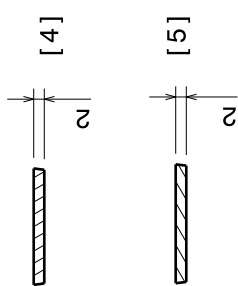
Therefore: $h \geq 2.6mm$

PART	DESCRIPTION	MATERIAL
[1]	SAMPLE PLATE	2404 DSS
[2]	MTR SPALL PLATE 1	2101 DSS
[3]	COVER PLATE	2101 DSS
[4]	SPALL PLATE 2	2101 DSS
[5]	SPALL PLATE 3	2101 DSS
[6]	MTR 2	2101 DSS
[7]	SAMPLE PLATE FOR PDV PROBE	2404 DSS
[8]	TARGET HOLDER	2101 DSS



NOTES:

- (A) REMOVE ALL BURRS BUT DO NOT BREAK CORNERS
- (B) ALL SURFACE FINISHES TO BE R0.4 MICROMETRES OR BETTER
- (C) LIGHT PRESS-FIT PART [1] INTO PART [2] WITH A VERY THIN COATING OF MOLYBDENUM GREASE ON ALL CONTACT SURFACES
- (D) MATCH ALL ANGLES OF PARTS [2], [3], [4], AND [5] WITH TAPER IN PART [6]
- (E) MATCH ANGLE OF PART [7] WITH TAPER IN PART [8]
- (F) LIGHT PRESS-FIT PARTS [2], [3], [4], AND [5] INTO PART [6] WITH VERY THIN COATING OF MOLYBDENUM GREASE ON ALL CONTACT SURFACES
- (G) LIGHT PRESS-FIT ASSEMBLY FROM NOTE (F) INTO PART [8] WITH VERY THIN COATING OF MOLYBDENUM GREASE ON ALL CONTACT SURFACES
- (H) LIGHT PRESS-FIT PART [7] INTO PART [8] WITH VERY THIN COATING OF MOLYBDENUM GREASE ON ALL CONTACT SURFACES
- (I) ENSURE FACES OF ASSEMBLED COMPONENTS ARE FLUSH



DESIGNED BY:	R Miller	I	-
DATE:	31/03/2018	H	-
CHECKED BY:	XXX	G	-
DATE:	XXX	F	-
SIZE	A3	E	-
SCALE	1:1	D	-
WEIGHT (kg)	XXX	C	-
DRAWING NUMBER	SRA 101	B	-
	1 / 1	A	31/03/2018

70mm Shock Recovery Assembly

UNSW Canberra

SRA 101

This drawing is our property; it can't be reproduced or communicated without our written agreement.

A

Shock-Recovery Assembly – Assembly Process

The assembly process for the Shock-Recovery Assembly (SRA) detailed in Table D1 is an important process due to the requirement for interfaces to resemble a continuous medium through which the shock wave can propagate without (or minimal) reflections. Molybdenum disulphide grease was used on all mating surfaces to aid in the assembly process. A Shimadzu 50kN press was used which allowed close monitoring of assembly forces and displacements for each step. This is vital to ensure the forces used maintain a safe margin from plastic strain for all components. The pressing rod, pressing/support ring, and supporting hole plate shown in the figures below are all customised pressing jigs for the assembly process.

Step #	Process	Force (kN)	Corresponding Figure
1	Sample Plate into MTR1/SP1	6	D1
2	Assembly from step 1 and Cover Plate into MTR2	6	D2
3	Spall Plate 2 and Spall Plate 3 into Assembly from step 2	20	D3
4	Assembly from step 4 into Target Holder	6	D4
5	Secondary (PDV) Sample into Target Holder	3	D5

Table D1. Assembly process for Shock-Recovery Assembly.

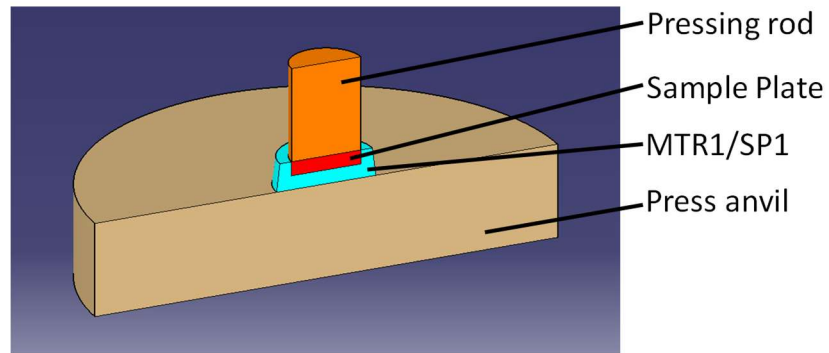


Figure D1. Assembly process Step 1.

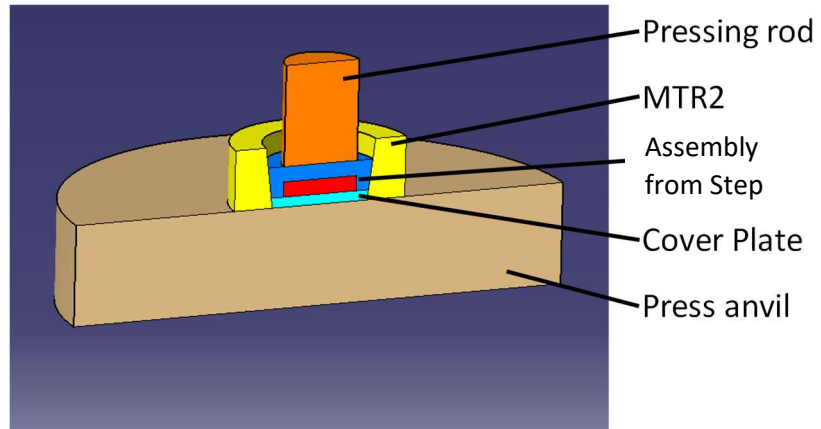


Figure D2. Assembly process Step 2.

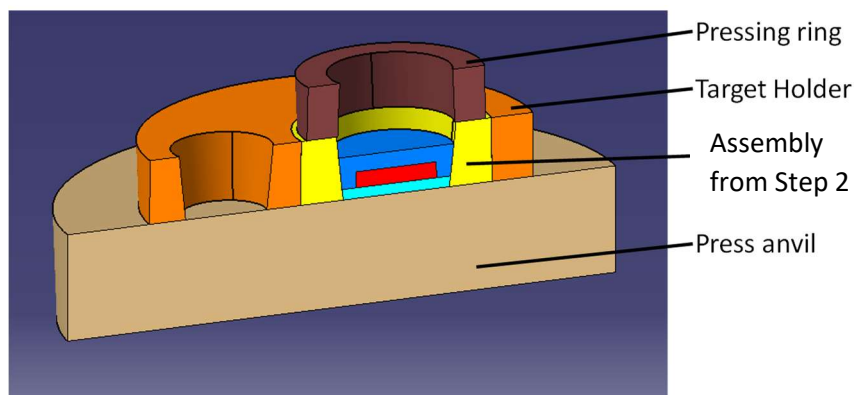


Figure D3. Assembly process Step 3.

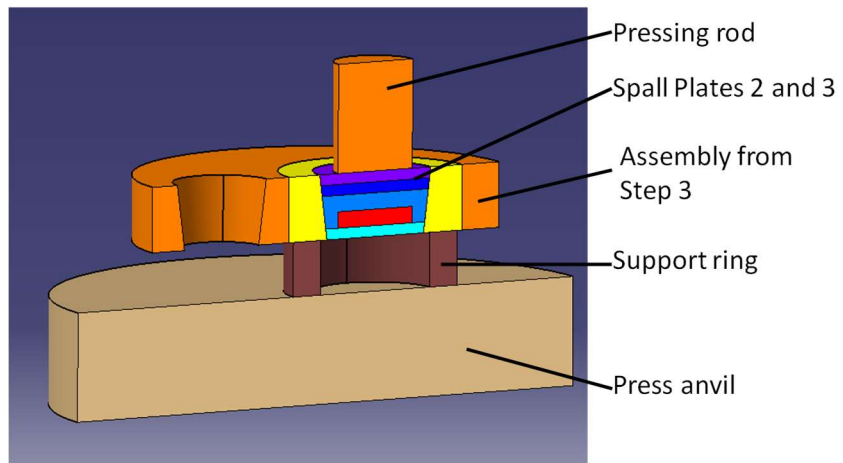


Figure D4. Assembly process Step 4.

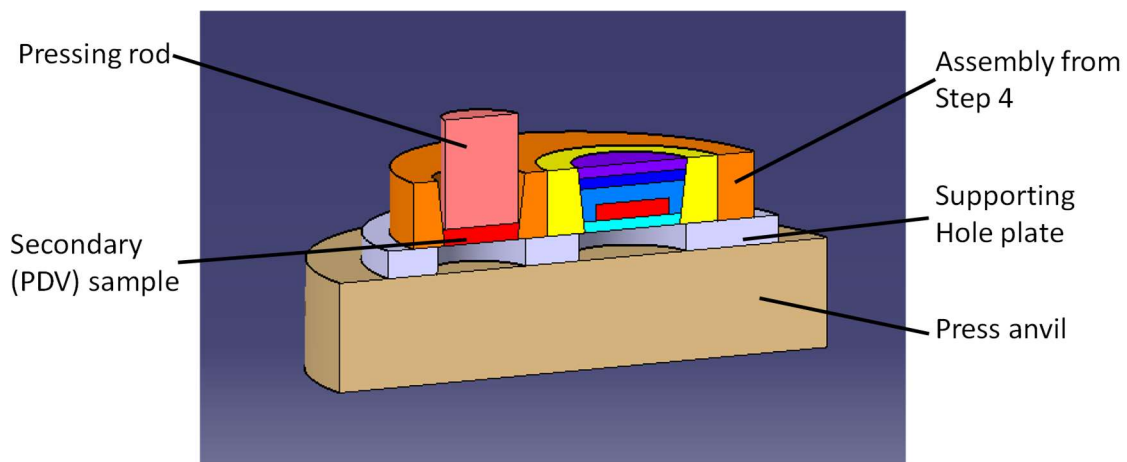


Image D5. Assembly process Step 5.

Post-Mortem Sample Preparation Process

Samples were prepared for analysis by cutting with a diamond saw along the appropriate plane as shown in Image E1. For the shock sample plate, this was on the central axis of the sample and parallel to the TD plane. The samples were held vertical in the mould using clips as seen in Image E2.



Image E1. Cutting the Sample and MTR1/SP1 in half on the diamond saw.

All samples were set in Struers Epofix mixed at a ratio of 25:3 by weight. Samples were marked to identify orientation from the parent plate and specific component within the Shock-Recovery Assembly as shown in Image E2. A standard Struers metallographic process was used to prepare the samples as detailed in Table E1. Samples were washed between steps using a Struers washer. Following the grinding and polishing process detailed in Table E1, the samples were polished further using a Buehler Vibro-polisher with MasterMet 0.02 μm non-crystallising colloidal silica polishing suspension for 3 hours at a vibration intensity of 50% and 400gram/sample weight.



Image E2. Sample plate half with label and clip to hold vertical, ready for setting in epoxy.

Step #	Process	Specifications	Force/sample	Time (minutes)	Comments
1	Grind	SiC Foil 320 + water	25N	6:00	Time varied to suit
2	Grind	SiC Foil 1000 + water	25N	0:40	
3	Polish	MD Largo + Diapro Allegro Largo #9	30N	6:00	5/8 rate for fluid
4	Polish	MD DAC + Diapro DAC 3 μm	20N	4:40	5/8 rate for fluid
5	Polish	MD Chem + OP-A 2 μm	15N	2:40	4/6 rate for fluid

Table E1. Grinding and polishing process followed for all sample preparation.